Supporting Information

FeNi-Layered Double-Hydroxide Nanoflakes with Potential for Intrinsically High Water-Oxidation Catalytic Activity

Manabu Ishizaki[1], Hiroya Tanno[1], Hikaru Sutoh[1], Tomohiro Katsuki[2], Taichi Hayasaka[2] Masayuki Yagi[2], Yuta Tsubonouchi[2], Kazuki Tajima[3], Tohru Kawamoto[3], Yusuke Sakuda[4], and Masato Kurihara[1]**

[1]Faculty of Science, Yamagata University, 1-4-12 Kojirakawa-machi, Yamagata, Yamagata 990-8560, Japan.

[2]Department of Materials Science and Technology, Faculty of Engineering, Niigata University, 8050 Ikarashi-2, Niigata 950-2181, Japan.

[3]Nanomaterials Research Institute, National Institute of Advanced Industrial Science and Technology (AIST), 1-1-1 Higashi, Tsukuba 305-8565, Japan.

[4]JEOL Ltd., 3-1-2, Musashino, Akishima, Tokyo 196-8558, Japan

*Manabu Ishizaki: e-mail, manabu-ishizaki@sci.kj.yamagata-u.ac.jp

Masato Kurihara: e-mail, kurihara@sci.kj.yamagata-u.ac.jp

KEYWORDS: *oxygen evolution reaction (OER), oxygen reduction reaction (ORR), carbon paper (CP), FeNi layered double hydroxide (LDH), Prussian-blue analog (PBA)*

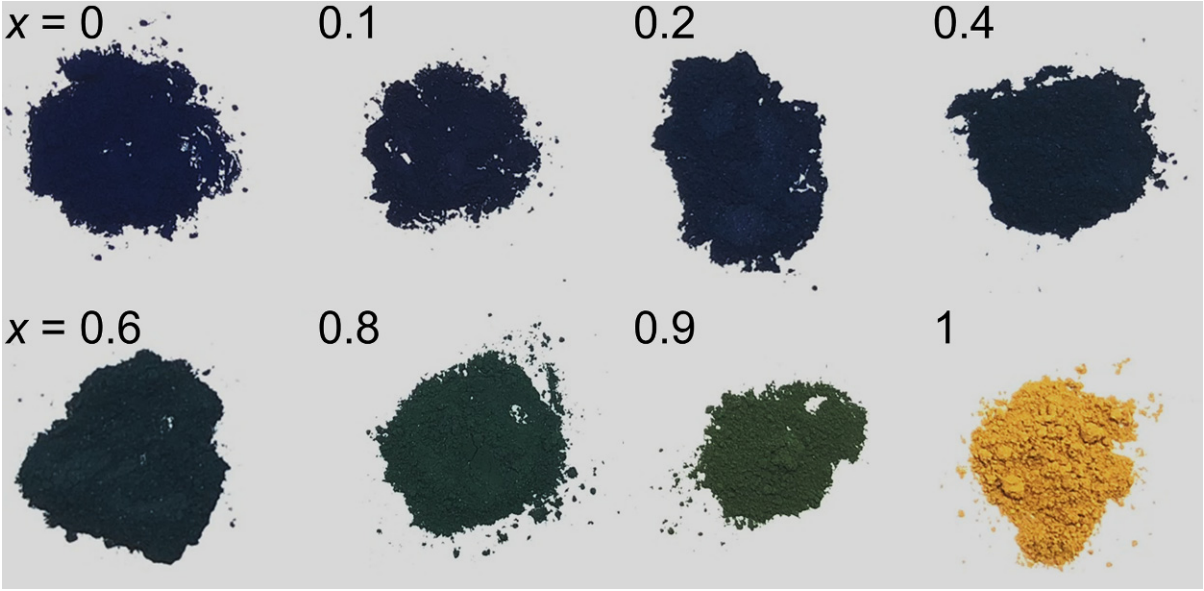

Figure S1. Photographs of the insoluble powdery solids of FeNi PBA NPs ($Fe_{1-x}Ni_x[Fe(CN)_6]_{0.67}{\cdot}yH_2O$).

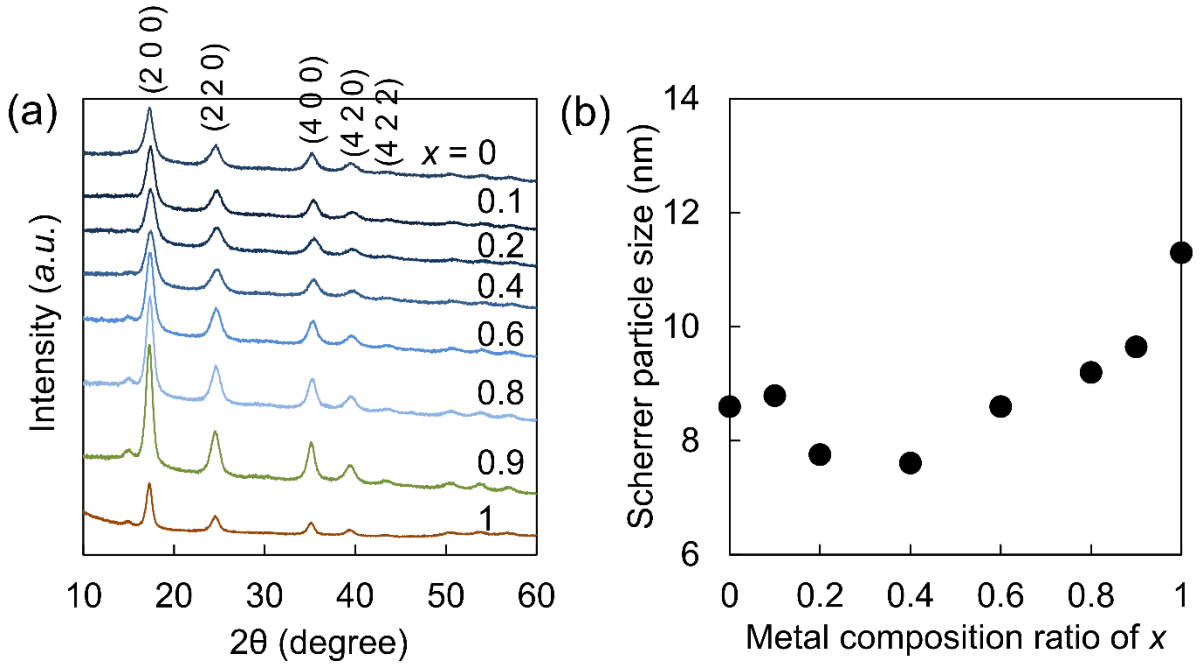

Figure S2. (a) XRD patterns of insoluble powdery solids of FeNi PBA NPs ($Fe_{1-x}Ni_x[Fe(CN)_6]_{0.67}{\cdot}yH_2O$). (b) Correlation between the metal composition ratios of x and the Scherrer particle sizes of the primary NPs estimated from half-height widths of the broadened XRD signals of (a).

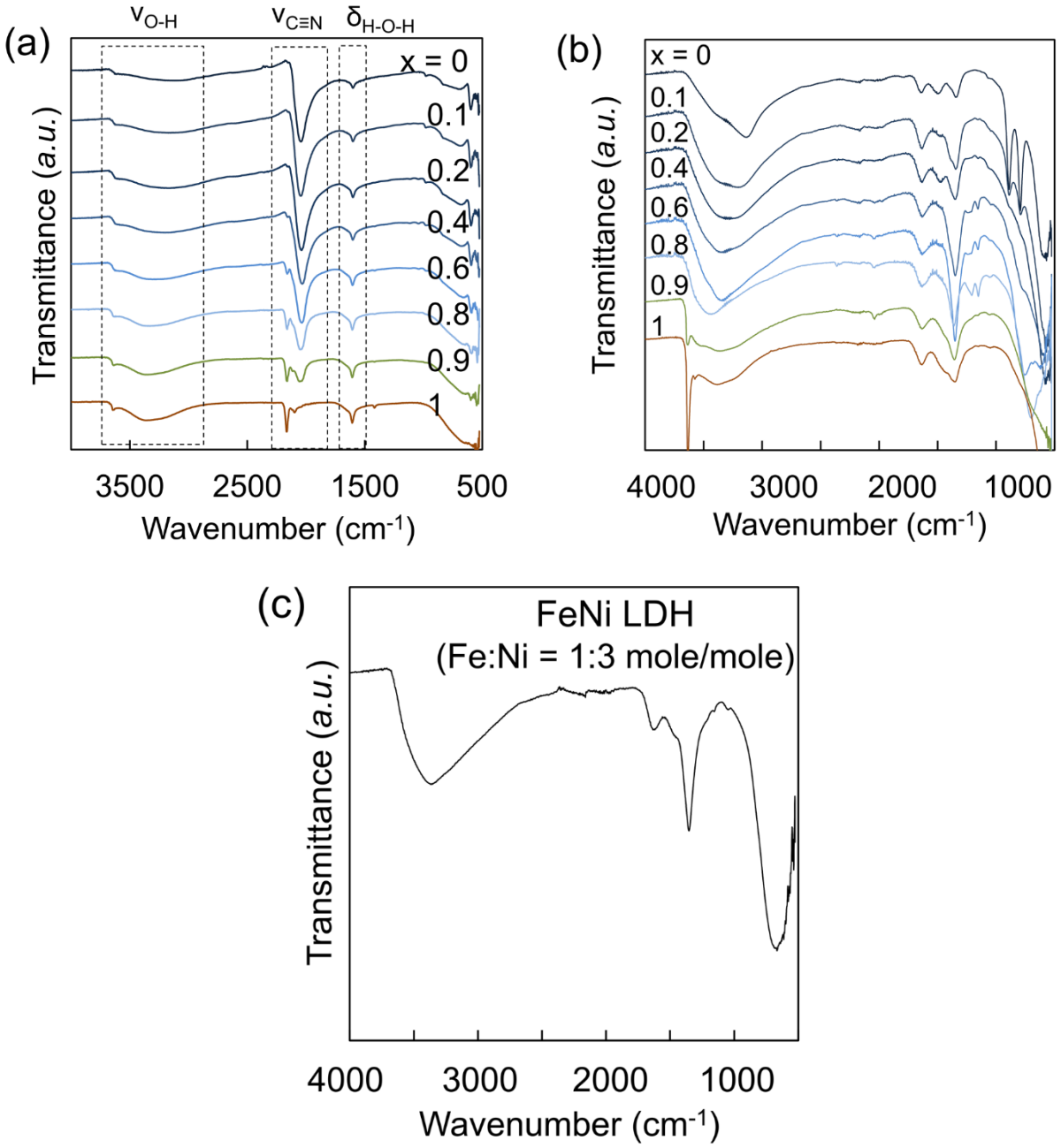

Figure S3. FT-IR spectra: (a) the insoluble powdery solids of FeNi PBA NPs ($Fe_{1-x}Ni_x[Fe(CN)_6]_{0.67}{\cdot}yH_2O$); (b) hydrolysis forms ($Fe_{1-x}Ni_xOHs$) transformed from FeNi PBA NPs in an aqueous solution of KOH (1.0 M); (c) FeNi LDH (Fe:Ni = 1:3 mole/mole).

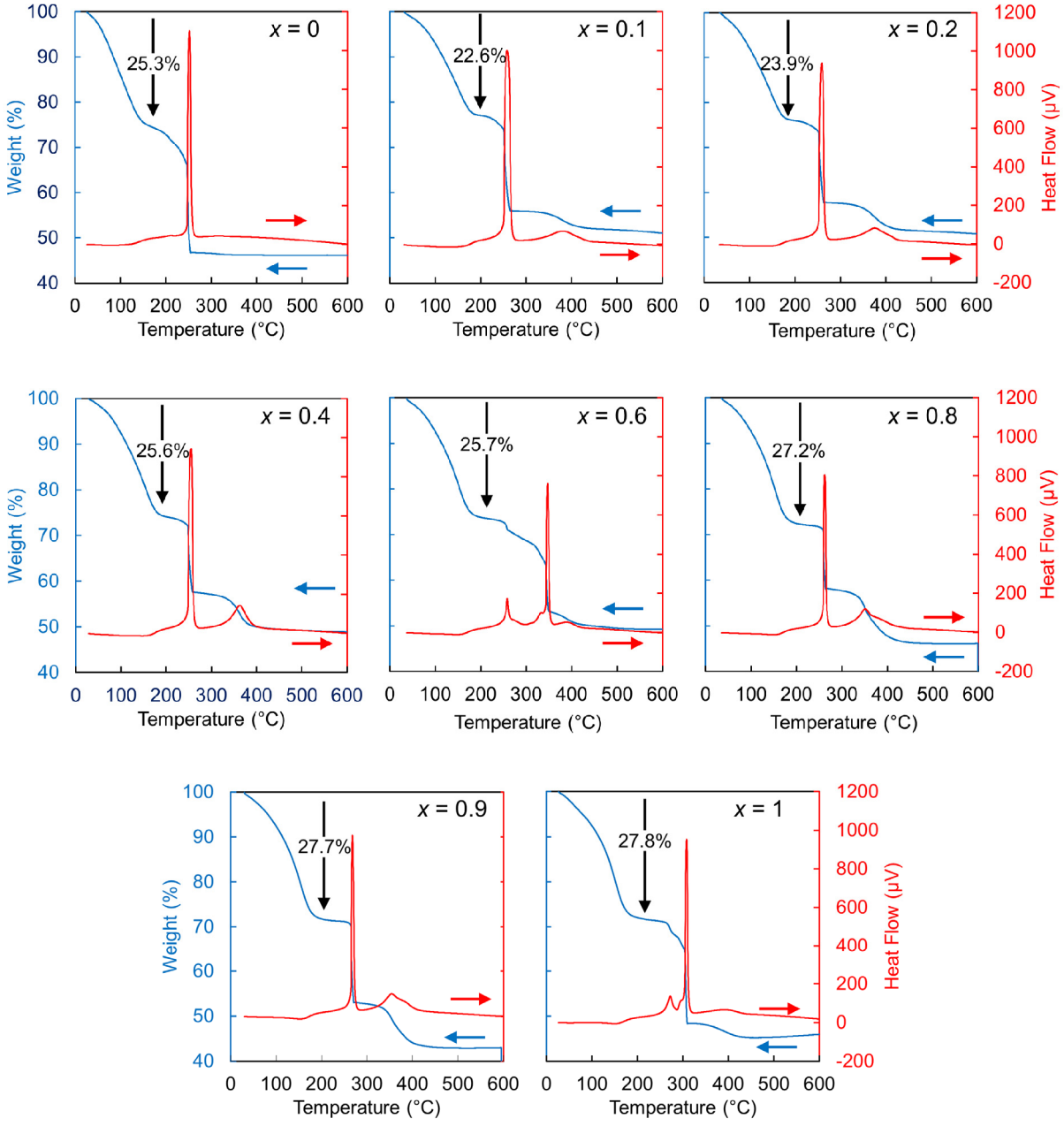

Figure S4. TG-DTA profiles of the insoluble powdery solids of FeNi PBA NPs ($Fe_{1-x}Ni_x[Fe(CN)_6]_{0.67}\cdot yH_2O$).

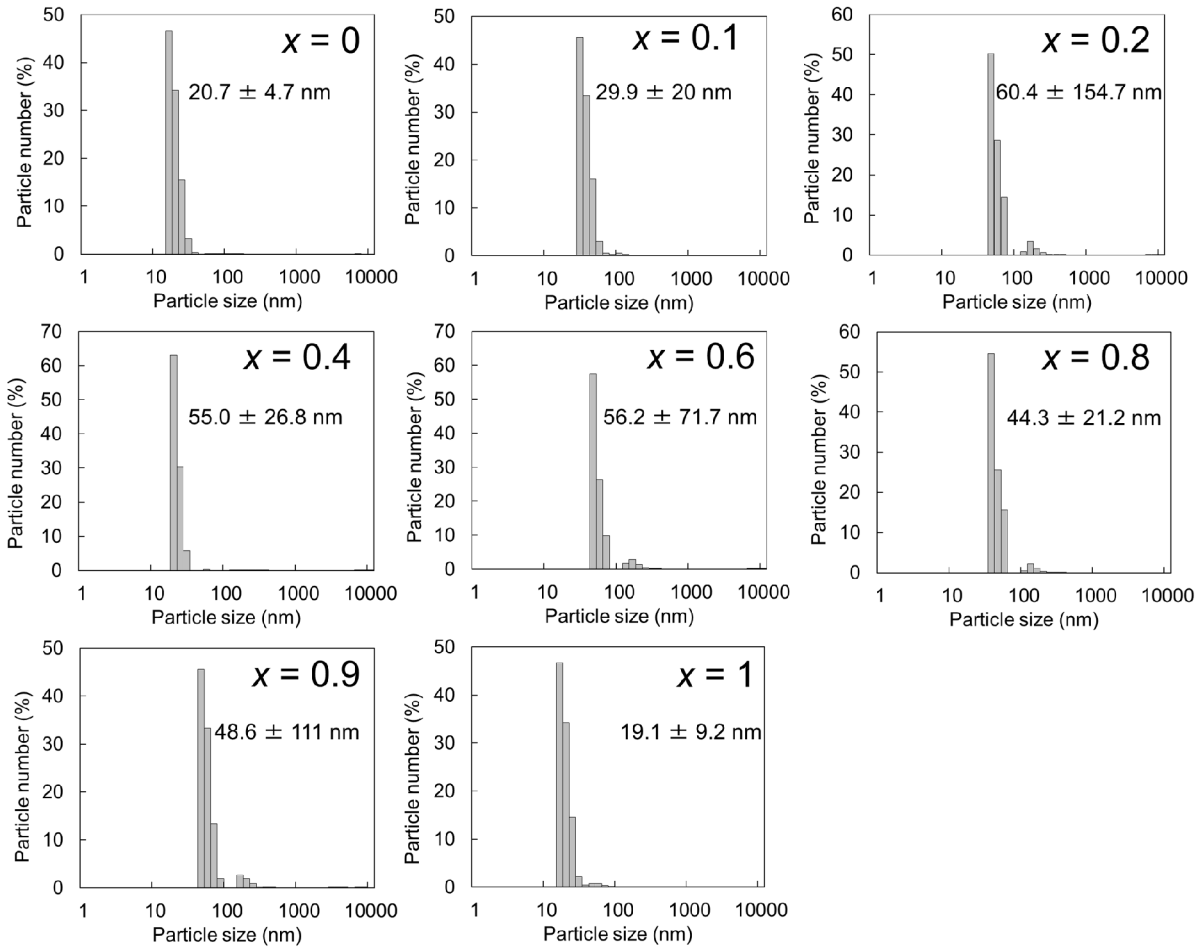

Figure S5. DLS particle-size distributions of surface-modified FeNi PBA NPs ($Fe_{1-x}Ni_x[Fe(CN)_6]_{0.67}{\cdot}yH_2O$) stably dispersed in water.

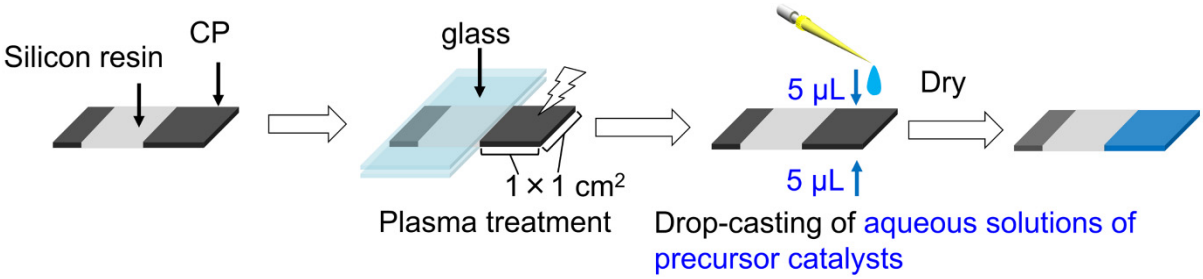

Figure S6. **Figure S6**. A schematic procedure for the immobilization of FeNi PBA NPs, FeNi LDHs, Mn^{2+}, or Ir^{3+} on CP. An aqueous dispersion solution of surface-modified FeNi PBA NPs, an aqueous suspension of FeNi LDHs, an aqueous solution of Mn^{2+}, or an aqueous solution of Ir^{3+} is drop-casted on a sheet of CP (see the experimental section).

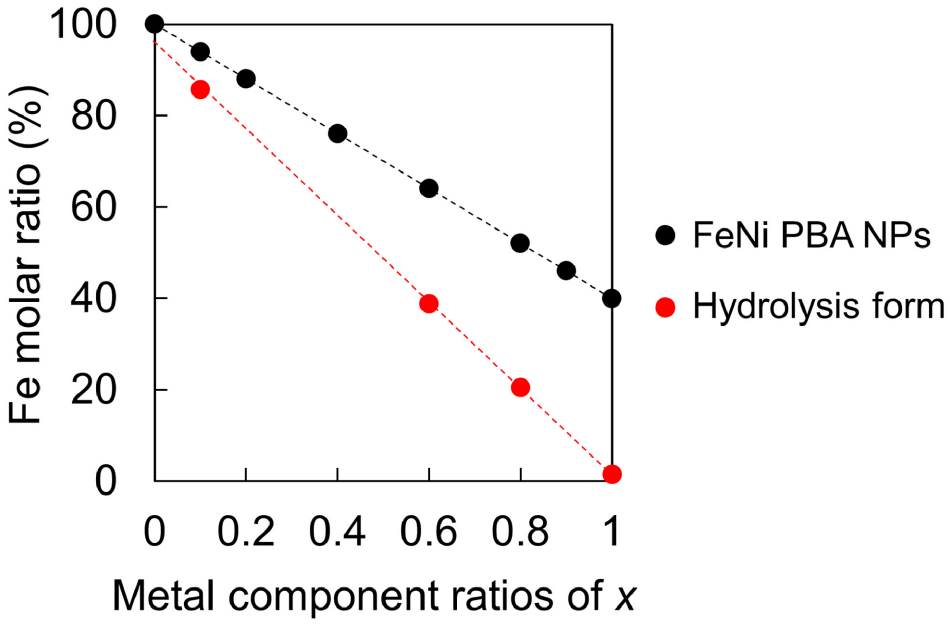

Figure S7. Fe molar ratios of insoluble powdery solids of FeNi PBA NPs ($Fe_{1-x}Ni_x[Fe(CN)_6]_{0.67}{\cdot}yH_2O$) (●) and their hydrolysis forms, $Fe_{1-x}Ni_xOHs$, isolated from an aqueous solution of KOH (1.0 M) (●). The Fe molar ratios are expressed by Fe/(Fe+Ni) × 100 (%).

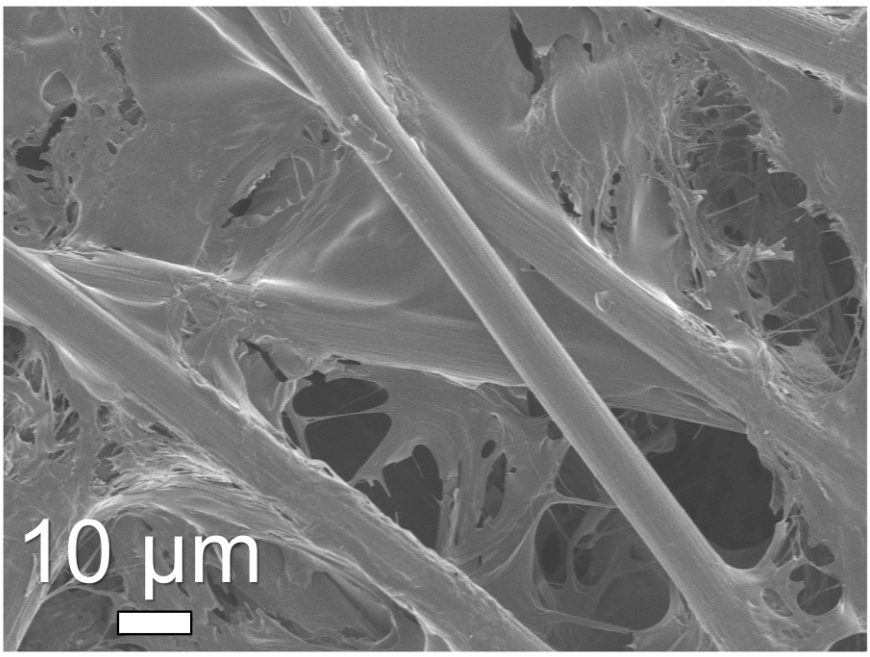

Figure S8. FE-SEM image of the carbon paper.

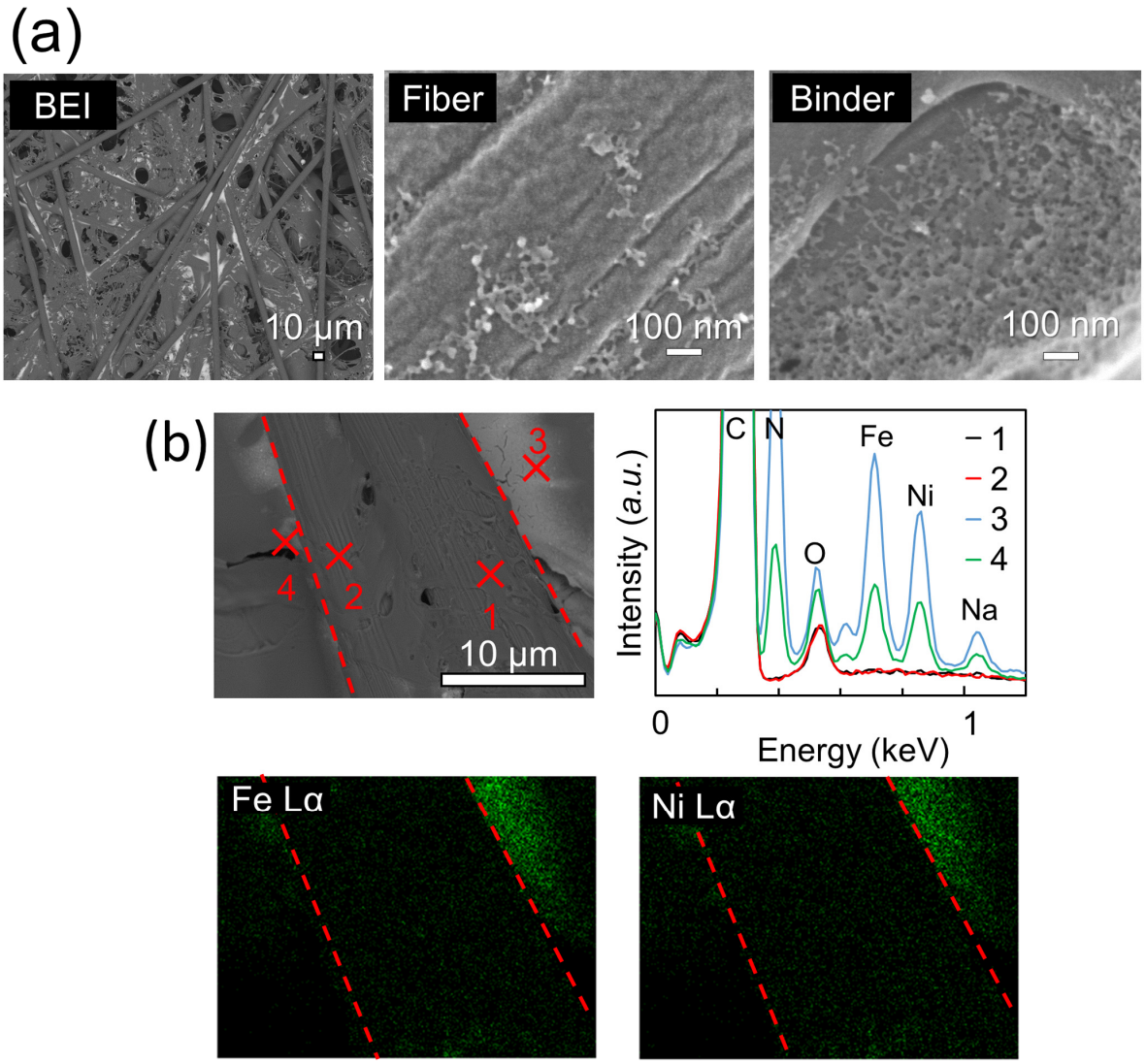

Figure S9. (a) FE-SEM (backscattered electron (BE)) image of surface-modified FeNi PBA NPs (x = 0.6) and their magnified FE-SEM images on wrinkles of the fiber and a dent of the binder. (b) SEM-EDS mapping and the point analysis of surface-modified FeNi PBA NPs (x = 0.6).

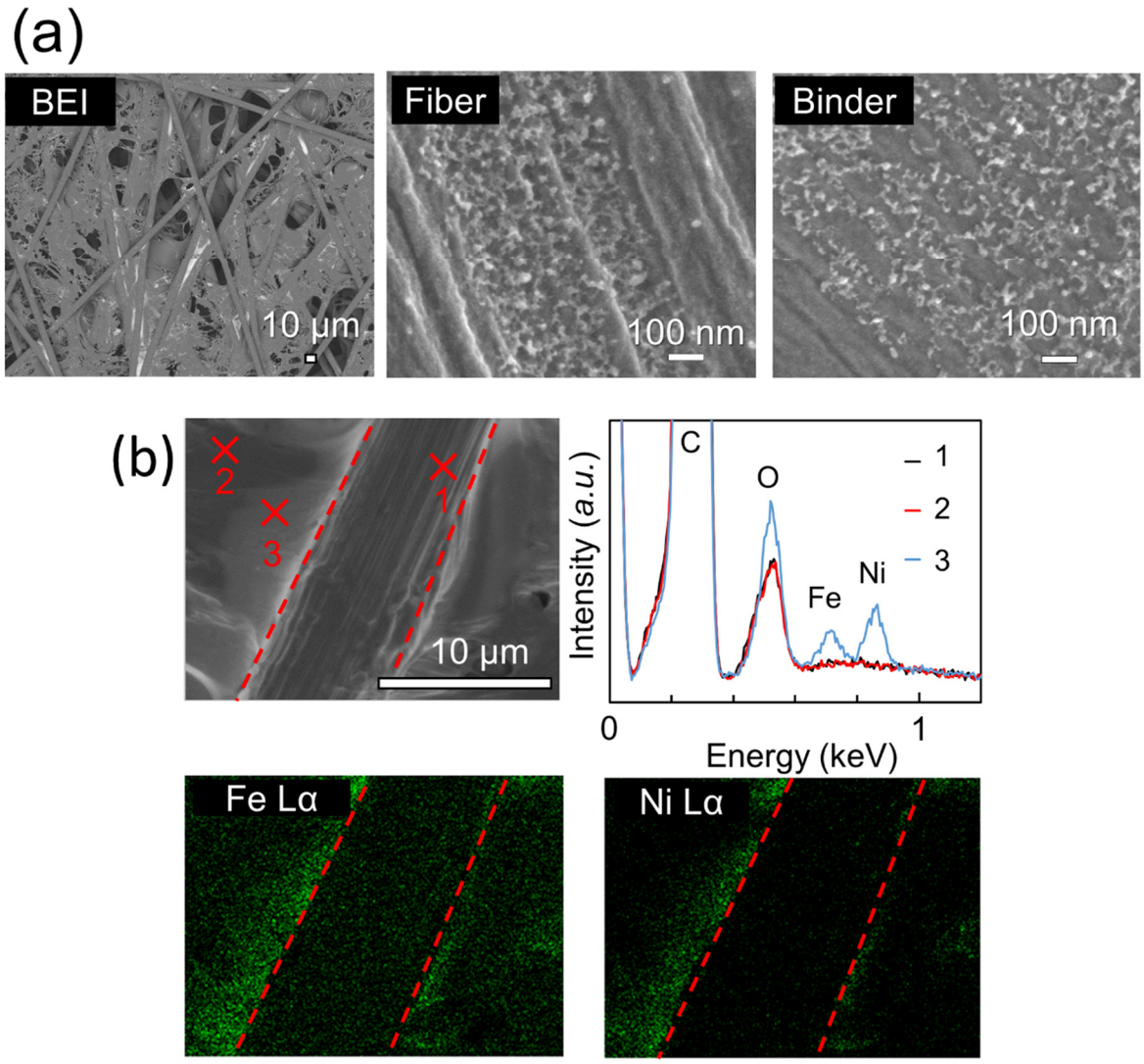

Figure S10. (a) FE-SEM (backscattered electron (BE)) image of $Fe_{0.4}Ni_{0.6}OH$ NPs and their magnified FE-SEM images on wrinkles of the fiber and a dent of the binder. (b) SEM-EDS mapping and the point analysis of $Fe_{0.4}Ni_{0.6}OH$ NPs. Red dashed lines indicate the boundaries between the fiber and the binder.

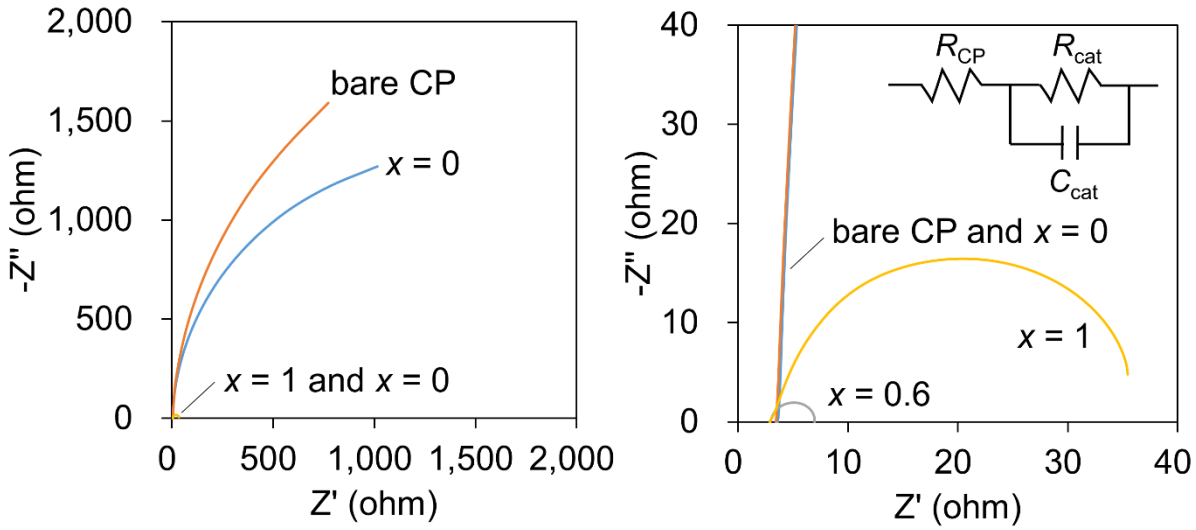

Figure S11. Nyquist plots of $Fe_{1-x}Ni_xOH$ NPs under the same mole-loading amount of 7.50 × 10^{-2} μmol on CP in the cases of x = 0, 0.6, and 1, where an applied potential is 1.51 V vs. RHE, near the OER onset potential catalyzed by $Fe_{0.4}Ni_{0.6}OH$ NPs (x = 0.6)

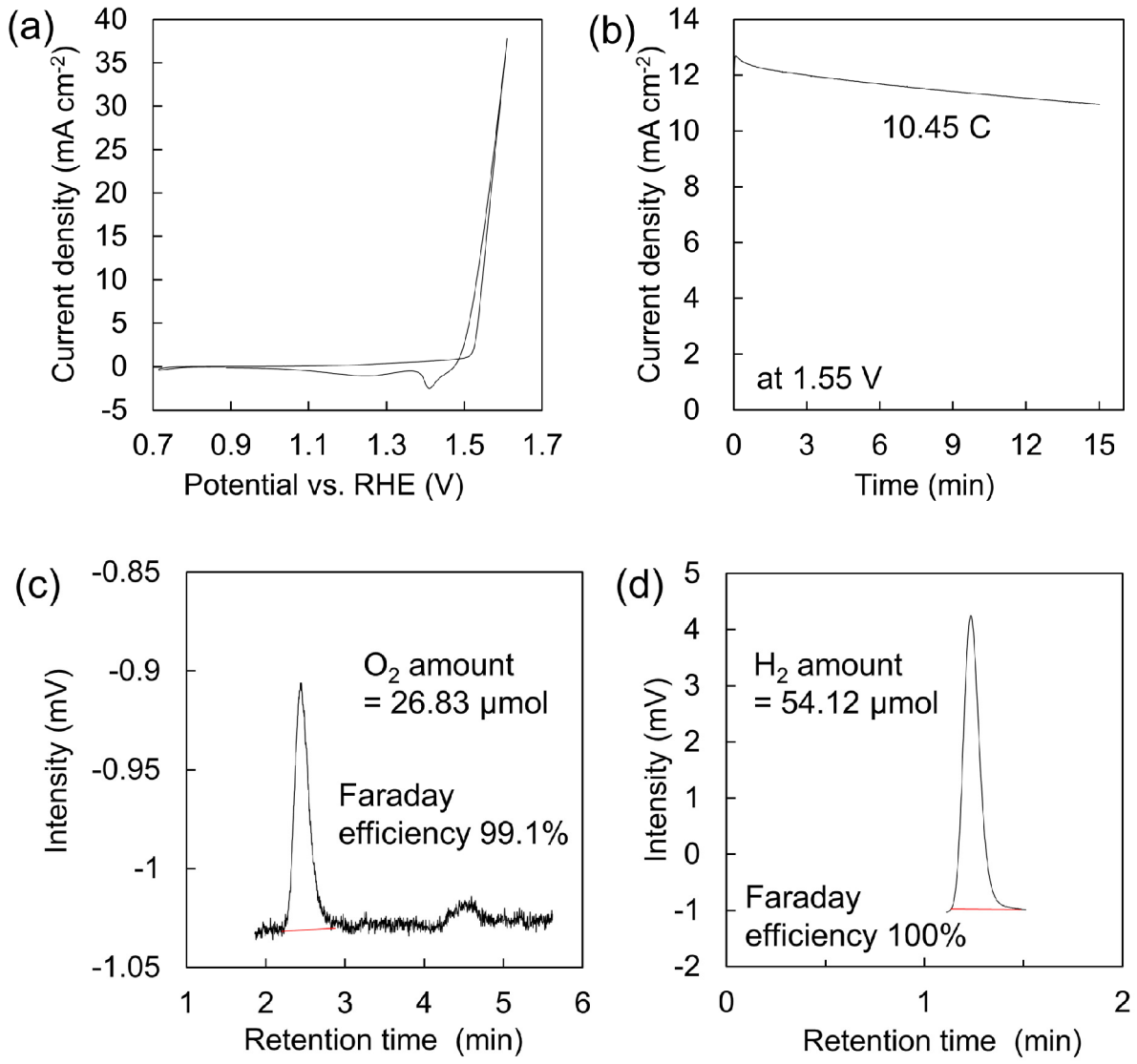

Figure S12. The OER Faraday efficiency: (a) CV at a scan rate of 50 mV s^{-1} of $Fe_{0.4}Ni_{0.6}$ LDH NPs transformed from FeNi PBA NPs (mass-loading amount of 7.38 µg cm^{-2}) on CP; (b) a chronoamperometry measurement at η_{OER} = 320 mV (1.55 V vs. RHE); (c,d) gas chromatographs of evolved gases from a working electrode (O_2) and a counter electrode (H_2).

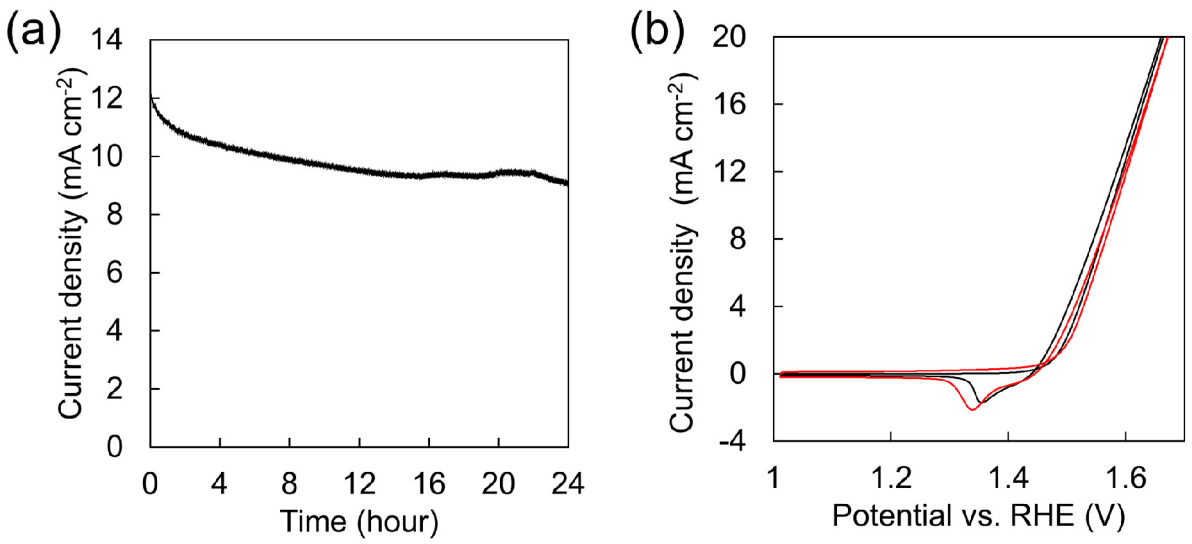

Figure S13. The OER catalytic durability: (a) a chronoamperometry measurement at η_{OER} = 330 mV (1.56 V vs. RHE) of $Fe_{0.4}Ni_{0.6}$ LDH NPs transformed from FeNi PBA NPs (mass-loading amount of 7.38 μg cm^{-2}) on CP; (b) CVs at a scan rate of 50 mV s^{-1} before (black line) and after (red line) the chronoamperometric measurement.

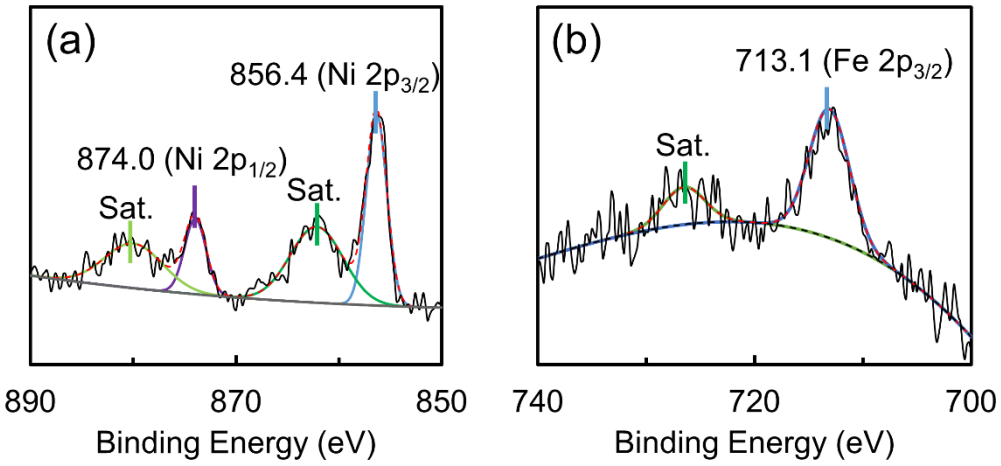

Figure S14. XPS analysis: (a) the binding energies of Ni atoms and (b) the binding energies of Fe atoms of $Fe_{0.4}Ni_{0.6}OH$ NPs after the OER catalytic durability experiment by chronoamperometry at η_{OER} = 330 mV (1.56 V vs. RHE) for 24 hours (Figure S13). The XPS spectra were not changed before (Figure 4b,d) or the OER catalytic durability experiment (Figure S13), indicating that the electronic structures of Fe and Ni atoms were maintained as an FeNi LDH structure during the OER experiment. The redox couples between Ni^{II} and Ni^{III} were anodically shifted as the metal composition ratios of Fe increased from x = 1 to 0.8. In the case of $Fe_{0.4}Ni_{0.6}OH$ NPs (x = 0.6), the Ni atom oxidation wave to Ni^{III} disappeared due to its coincidence with the OER catalytic current (Figure 5b). It is thought that the OER active Ni^{III} is an intermediate state and is immediately restored to the original stable state of Ni^{II} after the evolution of O_2.

Table S1. Comparison of OER catalytic activities

Catalysts (Fe/Ni molar ratios)	Electrodes	Mass-loading amounts (μg cm^{-2})	Tafel slopes (mV $dec.^{-1}$)	TOFs (s^{-1}) @ overpotentials, η_{OER} (mV)	Mass activities(A g^{-1}) @ overpotentials, η_{OER} (mV)	Overpotentials, η_{10} (mV)	Refs.
$Fe_{0.4}Ni_{0.6}$ LDH (0.67)	CP	7.38	15.1	0.023@250 0.15@260 0.36@270 1.57@300	157@250 974@260 2,400@270 10,600@300	269	This work
FeNi LDH (0.5)	CP Ni foam	200 200	40.3 ---	0.09@300 ---	--- ---	249 195	1
FeNi LDH/CNT (0.2)	CFP	250	31	0.56@300	10@228	247	2
FeNi LDH (0.6)	GC	50	21.2	---	200@260	260	3
FeNi LDH (0.33)	GC	70	40	0.05@300	---	302	4
FeNi LDH (0.52)	GC Ni foam	161.6 1,000	--- 52.8	0.013@300 ---	26.6@300 ---	--- 224	5
FeNi LDH/rGO (0.33)	Ni foam	250	39	0.99@300	---	206	6
a-FeNiOH (1.51)	CP	1.56	28	1.36@300	9,170@300	290	7
a-FeNiOH (0.97)	Ni foam	2,100	77	0.0004@250	0.79@250	323	8
a-FeNiOH/FeNiP (0.97)	Ni foam	1,800	39	0.036@250	93.3@250	199	8
$Fe_{0.55}Ni_{0.045}O_x$ (1.22)	GC	~5	35	0.14@300	600@300	320	9
Ni_xMnO_2	GC	280	60	0.061@400	46@400	400	10
NiCo LDH	GC	70	41	0.01@300	---	334	4
Ni_3N	GC CC	285 ---	45 41	--- ---	572@500 ---	--- 256	11
NiCeOH/G	GC	10,000	22	0.008@270	34.6@270	177	12
NiCeOH	GC	200	25	0.23@270	406.8@270	207	12
FeCo LDH	GC Ni foam	163.2 1,000	--- 92.0	0.0075@300 ---	17.7@300 ---	--- 288	5

FeLi LDH	GC Ni foam	129.3 1,000	--- 104.0	0.0054@300 ---	16.2@300 ---	--- 277	5
FeCoNiP	GC	60	66	0.47@300	---	200	13
CoS_2 NPs/N,S-doped GOx	GC	250	75	---	37.1@390	380	14
$Co_3O_4/NiCo_2O_4$	Ni foam	1,000	84	0.0287@350	---	320	15
$CuCo_2S_4$	GC	700	86	0.143@310	14.29@310	310	16
$YBaCo_4O_{7.3}$	GC	51	58	---	38.9@400	450	17
$Ba_{0.5}Sr_{0.5}Co_{0.8}Fe_{0.2}O_{3-\delta}$	Ni foil	1.4	70	---	9,006@500	490	18
Ir	GC Ni foam	160 1,000	--- 145.0	0.0036@300 ---	7.5@300 ---	--- 289	5
RuO_2	GC	200	47	0.006@270	26@270	290	13

a-; amorphous, CNT; carbon nanotube, G; graphite, GOx; graphene oxide, rGO; reduced graphene oxide, CP, carbon paper, GC, grassy carbon, CFP, carbon fiber paper, CC, carbon cloth. The following attached figure shows a schematic comparison of the OER catalytic activities based on the extracted data from Table S1, where a relationship between the applied overpotentials (η_{OER}) and the parameter values of mass activity, TOF, and Tafel slope is shown. The Tafel-slope values are relatively indicated by circle diameters, and the TOFs are indicated by color gradation. The smallest-diameter reddish circle located at the largest mass activity of this work means the highest intrinsic OER activity at an applied potential of η_{OER} = 300 mV.

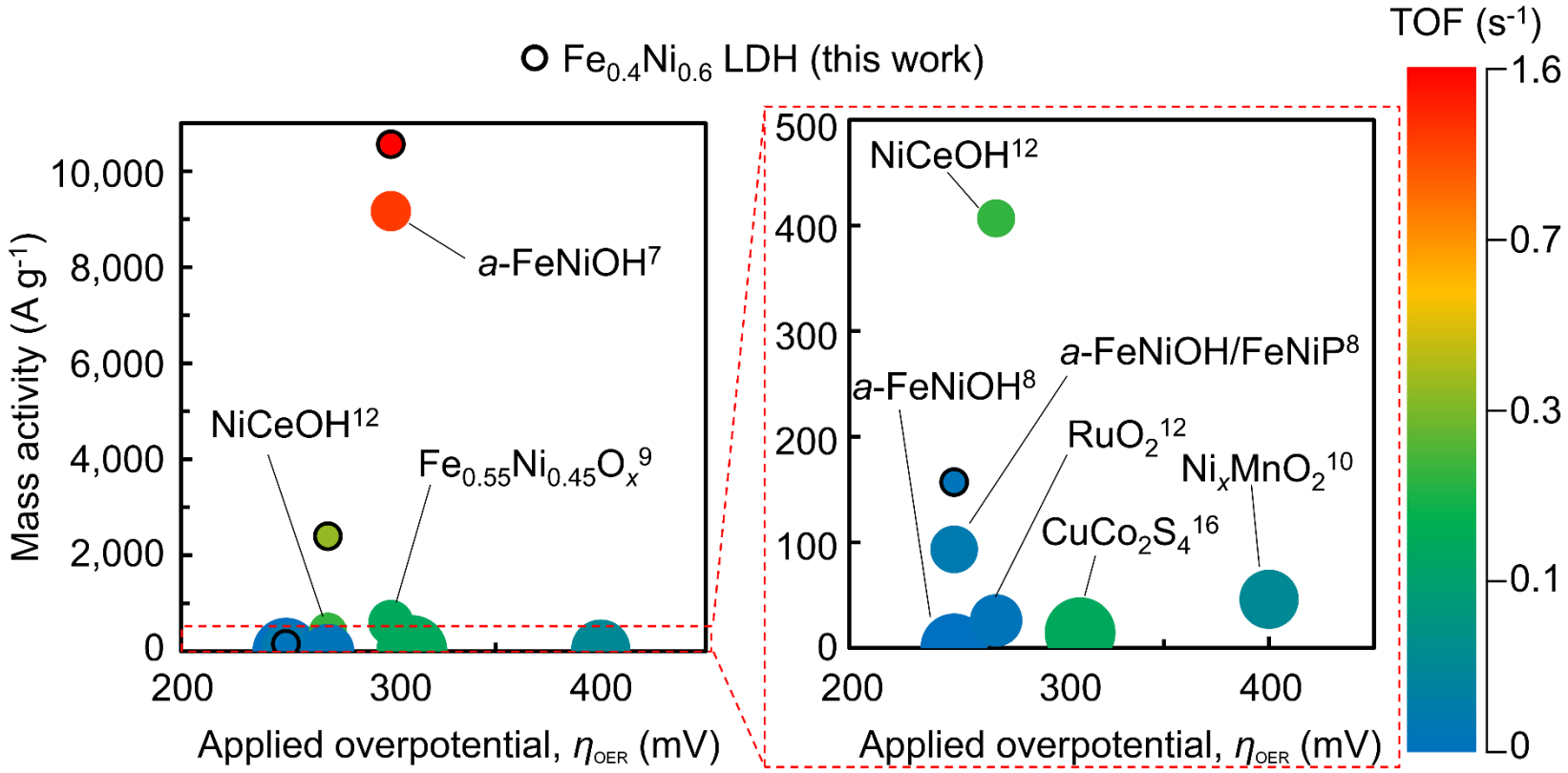

References in Table S1:

(1) Cai, Z.; Zhou, D.; Wang, M.; Bak, S. M.; Wu, Y.; Wu, Z.; Tian, Y.; Xiong, X.; Li, Y.; Liu, W.; Siahrostami, S.; Kuang, Y.; Yang, X. Q.; Duan, H.; Feng, Z.; Wang, H.; Sun, X., Introducing Fe^{2+} into Nickel-Iron Layered Double Hydroxide: Local Structure Modulated Water Oxidation Activity. *Angew. Chem. Int. Ed.* **2018**, *57*, 9392-9396.

(2) Gong, M.; Li, Y.; Wang, H.; Liang, Y.; Wu, J. Z.; Zhou, J.; Wang, J.; Regier, T.; Wei, F.; Dai, H., An Advanced Ni-Fe Layered Double Hydroxide Electrocatalyst for Water Oxidation. *J. Am. Chem. Soc.* **2013**, *135*, 8452-8455.

(3) Chen, R.; Sun, G.; Yang, C.; Zhang, L.; Miao, J.; Tao, H.; Yang, H.; Chen, J.; Chen, P.; Liu, B., Achieving Stable and Efficient Water Oxidation by Incorporating NiFe Layered Double Hydroxide Nanoparticles into Aligned Carbon Nanotubes. *Nanoscale Horiz.* **2016**, *1*, 156-160.
(4) Song, F.; Hu, X., Exfoliation of Layered Double Hydroxides for Enhanced Oxygen Evolution Catalysis. *Nat. Commun*. **2014**, *5*, 4477.
(5) Li, Z.; Shao, M.; An, H.; Wang, Z.; Xu, S.; Wei, M.; Evans, D. G.; Duan, X., Fast Electrosynthesis of Fe-containing Layered Double Hydroxide Arrays toward Highly Efficient Electrocatalytic Oxidation Reactions. *Chem. Sci.* **2015**, *6*, 6624-6631.
(6) Long, X.; Li, J.; Xiao, S.; Yan, K.; Wang, Z.; Chen, H.; Yang, S., A Strongly Coupled Graphene and FeNi Double Hydroxide Hybrid as an Excellent Electrocatalyst for the Oxygen Evolution Reaction. *Angew. Chem. Int. Ed.* **2014**, *53*, 7584-7588.
(7) Shi, Y.; Yu, Y.; Liang, Y.; Du, Y.; Zhang, B., In Situ Electrochemical Conversion of an Ultrathin Tannin Nickel Iron Complex Film as an Efficient Oxygen Evolution Reaction Electrocatalyst. *Angew. Chem. Int. Ed.* **2019**, *58*, 3769-3773.
(8) Liang, H.; Gandi, A. N.; Xia, C.; Hedhili, M. N.; Anjum, D. H.; Schwingenschlögl, U.; Alshareef, H. N., Amorphous NiFe-OH/NiFeP Electrocatalyst Fabricated at Low Temperature for Water Oxidation Applications. *ACS Energy Lett.* **2017**, *2*, 1035-1042.
(9) Görlin, M.; Chernev, P.; Ferreira de Araújo, J.; Reier, T.; Dresp, S.; Paul, B.; Krähnert, R.; Dau, H.; Strasser, P., Oxygen Evolution Reaction Dynamics, Faradaic Charge Efficiency, and the Active Metal Redox States of Ni-Fe Oxide Water Splitting Electrocatalysts. *J. Am. Chem. Soc.* **2016**, *138*, 5603-5614.
(10) Thenuwara, A. C.; Cerkez, E. B.; Shumlas, S. L.; Attanayake, N. H.; McKendry, I. G.; Frazer, L.; Borguet, E.; Kang, Q.; Remsing, R. C.; Klein, M. L.; Zdilla, M. J.; Strongin, D. R., Nickel Confined in the Interlayer Region of Birnessite: an Active Electrocatalyst for Water Oxidation. *Angew. Chem. Int. Ed.* **2016**, *55*, 10381-10385.
(11) Xu, K.; Chen, P.; Li, X.; Tong, Y.; Ding, H.; Wu, X.; Chu, W.; Peng, Z.; Wu, C.; Xie, Y., Metallic Nickel Nitride Nanosheets Realizing Enhanced Electrochemical Water Oxidation. *J. Am. Chem. Soc.* **2015**, *137*, 4119-4125.
(12) Yan, Z.; Sun, H.; Chen, X.; Liu, H.; Zhao, Y.; Li, H.; Xie, W.; Cheng, F.; Chen, J., Anion Insertion Enhanced Electrodeposition of Robust Metal Hydroxide/Oxide Electrodes for Oxygen Evolution. *Nat. Commun.* **2018**, *9*, 2373.
(13) Xu, J.; Li, J.; Xiong, D.; Zhang, B.; Liu, Y.; Wu, K. H.; Amorim, I.; Li, W.; Liu, L., Trends in Activity for the Oxygen Evolution Reaction on Transition Metal (M = Fe, Co, Ni) Phosphide Pre-catalysts. *Chem. Sci.* **2018**, *9*, 3470-3476.
(14) Ganesan, P.; Prabu, M.; Sanetuntikul, J.; Shanmugam, S., Cobalt Sulfide Nanoparticles Grown on Nitrogen and Sulfur Codoped Graphene Oxide: An Efficient Electrocatalyst for Oxygen Reduction and Evolution Reactions. *ACS Catal.* **2015**, *5*, 3625-3627.
(15) Yang, M.; Lu, W.; Jin, R.; Liu, X.-C.; Song, S.; Xing, Y., Superior Oxygen Evolution Reaction Performance of Co_3O_4/$NiCo_2O_4$/Ni Foam Composite with

Hierarchical Structure. *ACS Sustainable Chem. Eng.* **2019**, *7*, 12214-12221.

(16) Chauhan, M.; Reddy, K. P.; Gopinath, C. S.; Deka, S., Copper Cobalt Sulfide Nanosheets Realizing a Promising Electrocatalytic Oxygen Evolution Reaction. *ACS Cata.* **2017**, *7*, 5871-5879.

(17) Kirsanova, M. A.; Okatenko, V. D.; Aksyonov, D. A.; Forslund, R. P.; Mefford, J. T.; Stevenson, K. J.; Abakumov, A. M., Bifunctional OER/ORR Catalytic Activity in the Tetrahedral $YBaCo_4O_{7.3}$ Oxide. *J. Mater. Chem. A* **2019**, *7*, 330-341.

(18) Chen, G.; Zhou, W.; Guan, D.; Sunarso, J.; Zhu, Y.; Hu, X.; Zhang, W.; Shao, Z., Two Orders of Magnitude Enhancement in Oxygen Evolution Reactivity on Amorphous $Ba_{0.5}Sr_{0.5}Co_{0.8}Fe_{0.2}O_{3-\delta}$ Nanofilms with Tunable Oxidation State. S*ci. Adv.* **2017**, *3*, e1603206.

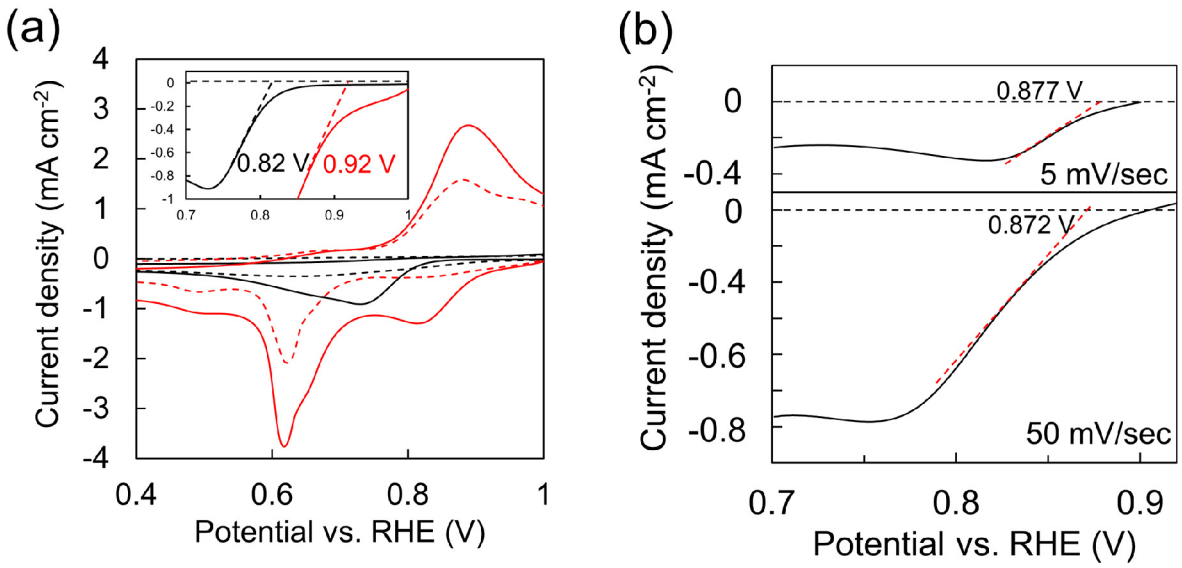

Figure S15. (a) CVs of the plasma-treated CP (black lines) and Mn-immobilized CP (red lines) after Ar bubbling (dash line) or O_2 bubbling (solid line). The insert figure shows the onset potential. (b) LSVs and onset potentials of Mn-immobilized CP at different scan rates.

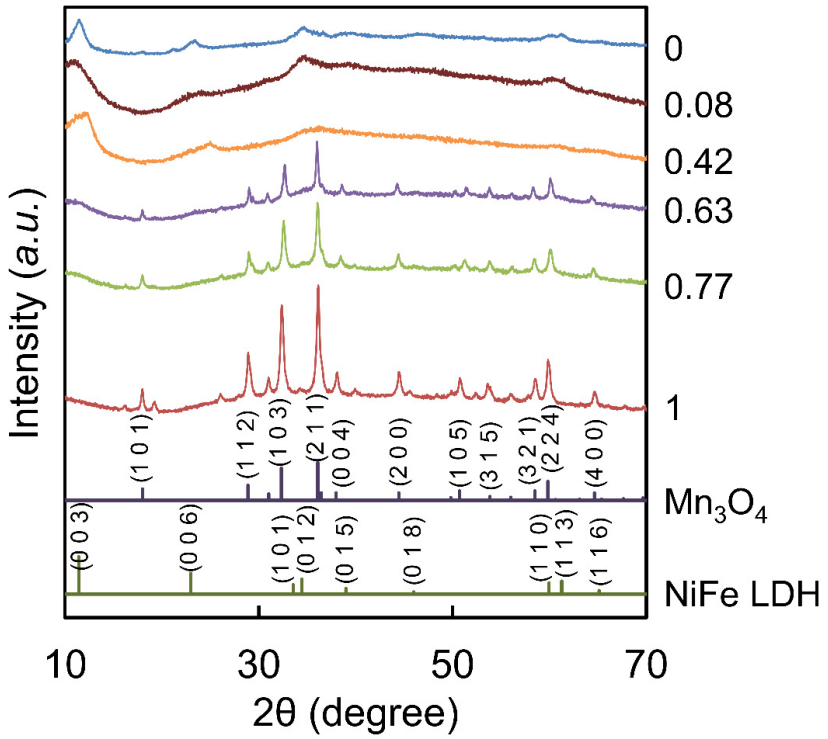

Figure S16. XRD patterns of the Fe-Ni-Mn ternary-metal species precipitated from FeNi PBA NPs ($x = 0.6$) mixed with an aqueous solution of Mn^{2+} after the addition of an aqueous solution of KOH (1.0 M), where the metal-based molar ratios are Mn/(Fe+Ni+Mn). In the absence of Mn^{2+} and FeNi PBA NPs, Mn/(Fe+Ni+Mn) is 0 and 1, respectively.

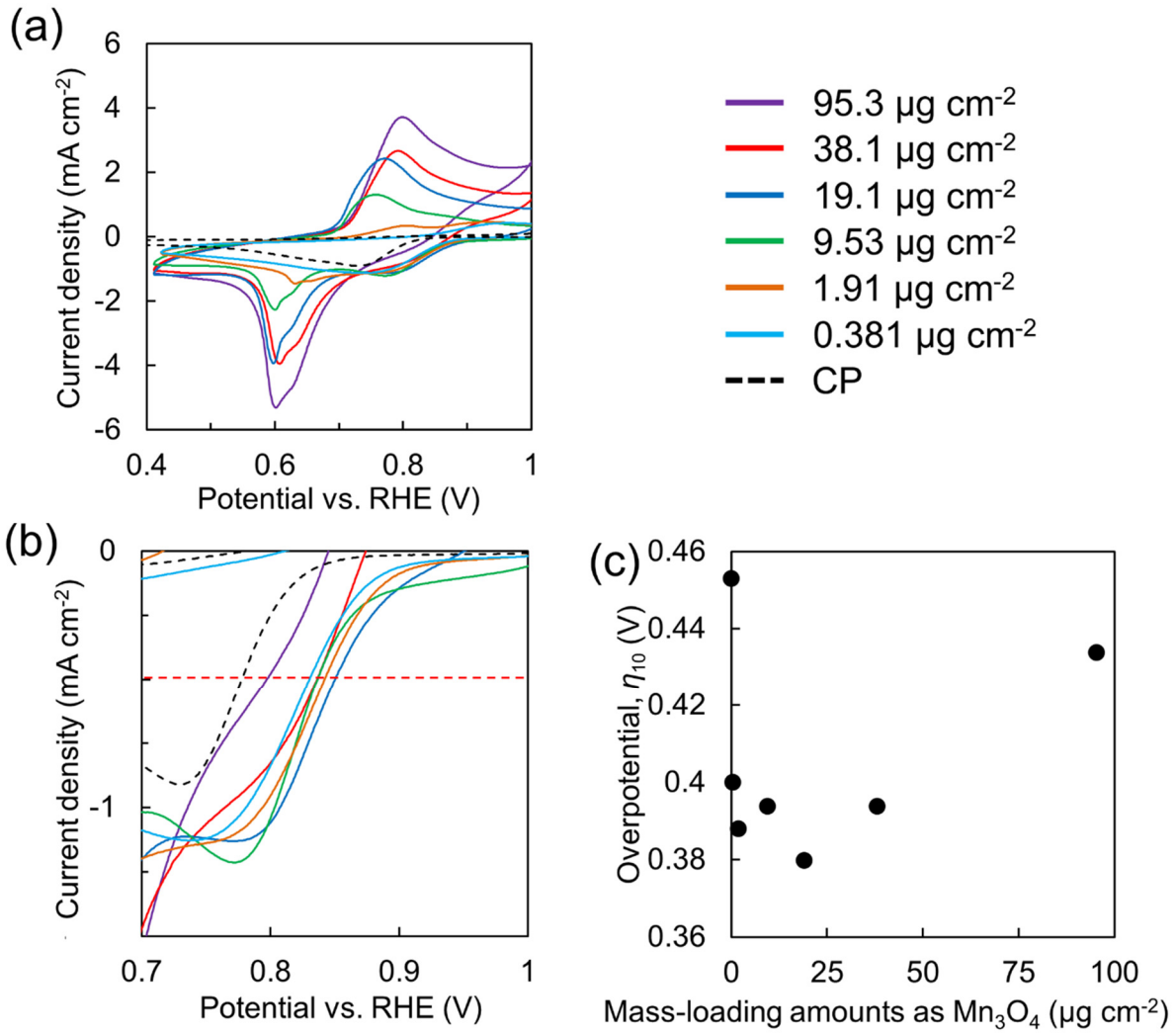

Figure S17. a) CVs of Mn-immobilized CP depending on mass-loading amounts calculated as Mn_3O_4. (b) Magnified ORR currents of (a). (c) The relationship between overpotentials at -0.5 $mA \cdot cm^{-2}$ and the mass-loading amounts.

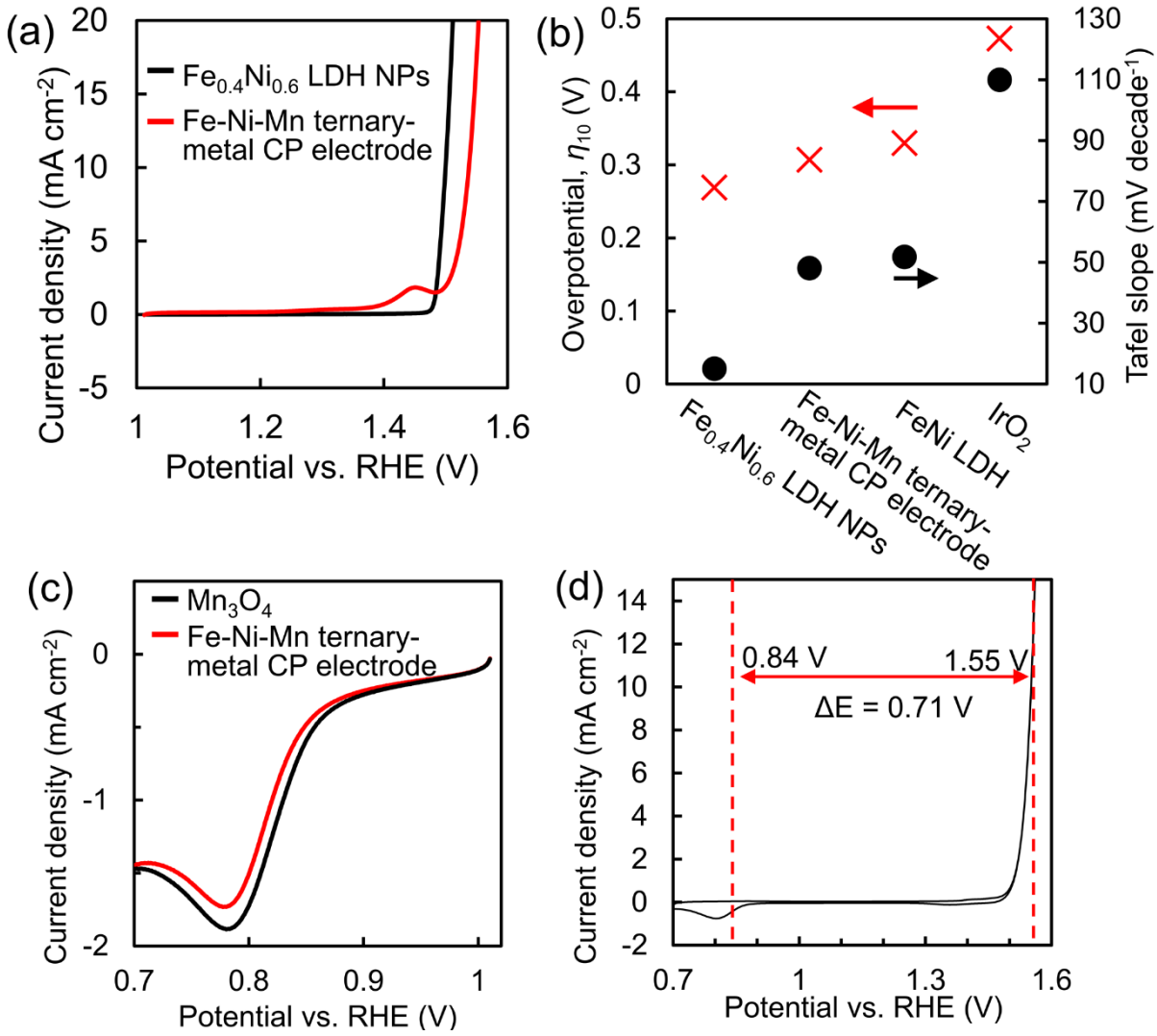

Figure S18. Pseudo bifunctional OER and ORR activities of a Mn-Fe-Ni ternary-metal CP electrode: (a) *iR*-corrected LSVs in an OER applied potential range at a scan rate of 5 mV s^{-1} for $Fe_{0.4}Ni_{0.6}$ LDH NPs on a CP electrode and a Mn-Fe-Ni ternary-metal CP electrode; (b) plots of normalized OER overpotentials, η_{10} (×), and Tafel-slop values (●) estimated from (a); (c) *iR*-corrected LSVs in an ORR applied potential range at a scan rate of 50 mV s^{-1} for Mn_3O_4 on a CP electrode and a Mn-Fe-Ni ternary-metal CP electrode; (d) full-range *iR*-corrected CV with OER and ORR catalytic currents at a scan rate of 5 mV s^{-1} for a Mn-Fe-Ni ternary-metal CP electrode showing a pseudo OER and ORR bifunction.

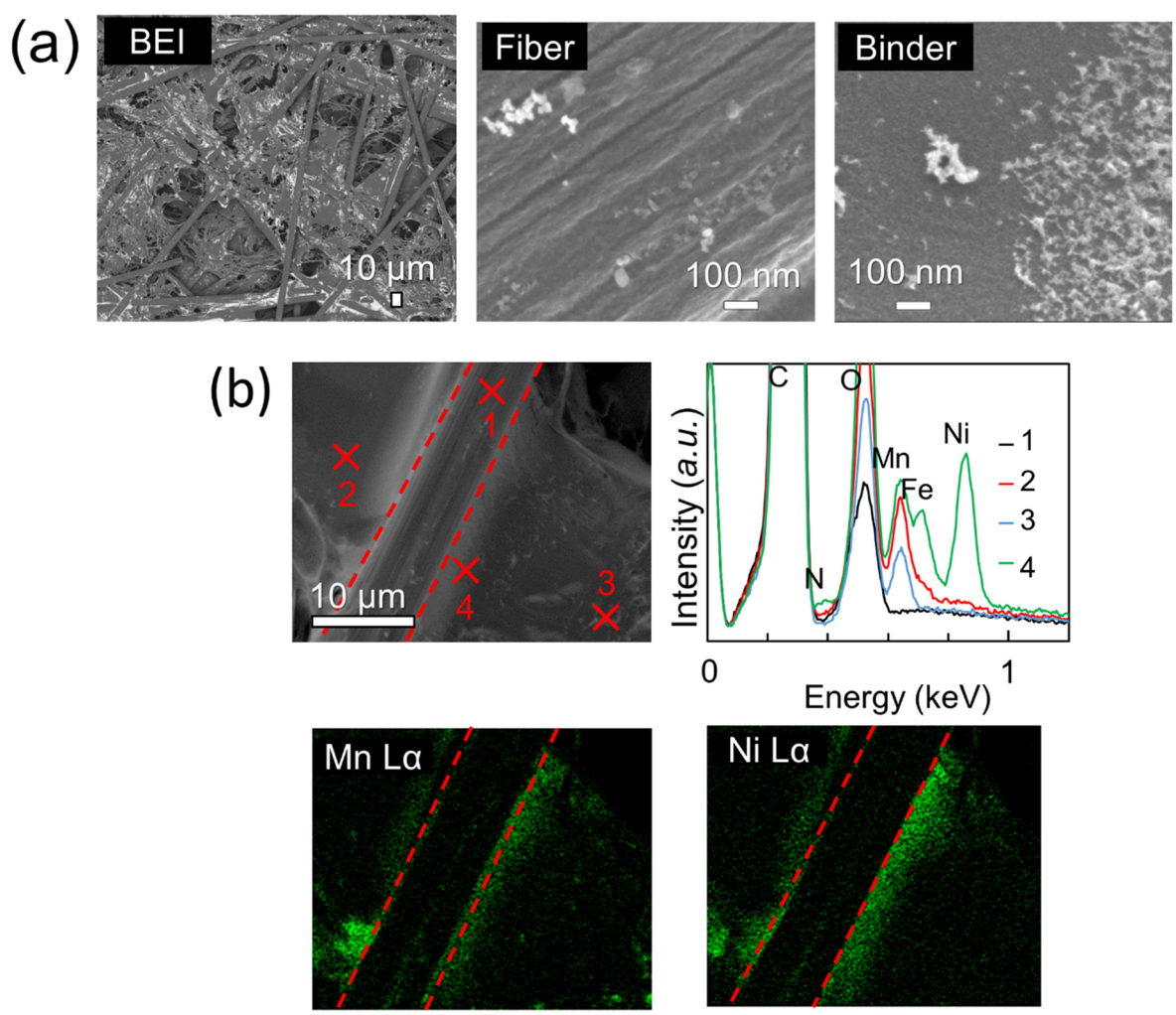

Figure S19. (a) FE-SEM (backscattered electron (BE)) image of the Fe-Ni-Mn ternary-metal CP electrode and their magnified FE-SEM images on wrinkles of the fiber and a dent of the binder. (b) SEM-EDS mapping and the point analysis of the Fe-Ni-Mn ternary-metal CP electrode. Red dashed lines indicate the boundaries between the fiber and the binder.